ADVANCED HEALTHCARE MATERIALS
www.advhealthmat.de

Next-Gen Poly(ϵ-Caprolactone) Scaffolds: Non-Destructive In Vivo Monitoring and Accelerated Biodegradation

Kristyna Kolouchova, Quinten Thijssen, Ondrej Groborz, Lana Van Damme, Jana Humajova, Petr Matous, Astrid Quaak, Martin Dusa, Jan Kucka, Ludek Sefc, Martin Hruby, and Sandra Van Vlierberghe**

Poly(ε-caprolactone) (PCL) is a biocompatible, biodegradable, and highly mechanically resilient FDA-approved material (for specific biomedical applications, e.g. as drug delivery devices, in sutures, or as an adhesion barrier), rendering it a promising candidate to serve bone tissue engineering. However, in vivo monitoring of PCL-based implants, as well as biodegradable implants in general, and their degradation profiles pose a significant challenge, hindering further development in the tissue engineering field and subsequent clinical adoption. To address this, photo-cross-linkable mechanically resilient PCL networks are developed and functionalized with a radiopaque monomer, 5-acrylamido-2,4,6-triiodoisophthalic acid (AATIPA), to enable non-destructive in vivo monitoring of PCL-based implants. The covalent incorporation of AATIPA into the crosslinked PCL networks does not significantly affect their crosslinking kinetics, mechanical properties, or thermal properties, but it increases their hydrolysis rate and radiopacity. Complex and porous 3D designs of radiopaque PCL networks can be effectively monitored in vivo. This work paves the way toward non-invasive monitoring of in vivo degradation profiles and early detection of potential implant malfunctions.

1. Introduction

PCL has emerged as a highly promising synthetic biomaterial for the engineering of hard tissues in the field of regenerative medicine.[1,2] PCL is biodegradable and takes 2–5 years to fully degrade in vivo, depending on factors such as pH, implant location, inflammation, enzymatic activity, and other parameters.[3,4] Moreover, it is mechanically stable (ultimate strength > 23 MPa), rendering it a promising candidate for the development of biodegradable implants serving bone tissue engineering.[5] Furthermore, PCL-based materials can be 3D printed via extrusion-based 3D-printing (thermoplastic PCL) or light-based 3D-printing methods (when exploiting photo-curable PCL derivatives) and, therefore, they can replicate the 3D structure and porosity of the targeted tissue type. Final, PCL-based biomaterials can be modified to introduce cell-adhesivity[6,7] toward tissue engineering of hard tissues such as bone or cartilage.[8,9]

Although PCL-based implants are exceptionally promising to serve tissue engineering, currently, monitoring their degradation in vivo is challenging, which hinders the development of materials with specific biodegradation rates. So far, most biodegradation data collected from studies encompassing biodegradable materials originate solely from ex vivo destructive examinations,[10–16] which provide data only within a limited time frame, are costly,

K. Kolouchova, Q. Thijssen, L. Van Damme, A. Quaak, S. Van Vlierberghe
Polymer Chemistry and Biomaterials Group
Department of Organic and Macromolecular Chemistry
Centre of Macromolecular Chemistry
Ghent University
Krijgslaan 281, Building S4, Belgie, Ghent 9000, Belgium
E-mail: Kristyna.Kolouchova@UGent.be;
Sandra.VanVlierberghe@UGent.be

The ORCID identification number(s) for the author(s) of this article can be found under https://doi.org/10.1002/adhm.202402256

DOI: 10.1002/adhm.202402256

O. Groborz
Institute of Biophysics and Informatics
First Faculty of Medicine
Charles University
Salmovská 1, Prague 2, Prague 12000, Czech Republic

O. Groborz
Institute of Organic Chemistry and Biochemistry
Czech Academy of Sciences
Flemingovo sq. 2, Prague 6, Prague 16000, Czech Republic

J. Humajova, P. Matous, M. Dusa, L. Sefc
Center for Advanced Preclinical Imaging (CAPI)
First Faculty of Medicine
Charles University
Salmovská 3, Prague 2, Prague 12000, Czech Republic

J. Kucka, M. Hruby
Institute of Macromolecular Chemistry
Czech Academy of Sciences
Heyrovského sq. 2, Prague 6, Prague 16206, Czech Republic

and cannot be translated to clinical practice. In the case of PCL-based materials specifically designed for bone tissue regeneration, some studies alternatively rely on radiological detection of bone fracture and its closure over time as an indirect proof of PCL degradation.[15,16] Alternative to this approach is to directly incorporate a diagnostic modality into the implant. Several studies have reported on PCL-based biomaterials that can be visualized using near-infrared (NIR) fluorescence imaging,[17,18] or ultrasound imaging.[12,13] Nonetheless, these imaging techniques have a limited penetration depth (3.2 cm for in vivo NIR fluorescence,[19] 1–5 cm for US[20]). Additionally, radiopaque PCLs with embedded tantalum(V) oxide (TaOx),[21] zirconium(IV) oxide,[22] or iodine carbon nanoparticles (ICPs)[23] for radioimaging were described. However, the nanoparticles can leach out from the crosslinked materials, thereby preventing long-term monitoring. Another study used a similar approach by employing iodixanol, a clinical contrast agent, blended within thermoplastic PCL electrospun fibers.[24] Conversely, a radiodense iodinated compound covalently linked to a degradable polyester, poly(caprolactone-co-1-4-oxepan-1,5-dione), has been described.[25] In that study, the degradable composite witnessed a relatively fast contrast decrease (30% over 8 weeks after implantation), impairing the long-term monitoring of implant fate.

From the above-mentioned diagnostic techniques, radiology techniques are inexpensive, readily available, and time-effective. Moreover, they are characterized by a high penetration depth and are safe for clinical use. However, radiology techniques solely permit the visualization of those materials whose radiopacity (radiopacity, i.e., absorbing X-ray) is significantly different from the surrounding tissues. Generally, the higher the proton number (Z) of the atoms present in the sample, the more the material absorbs X-rays due to the higher electron density in the electron shell near the atom nucleus. Iodinated aromatic compounds are especially useful as radiopaque X-ray contrast agents as iodine has a high Z and – in this chemical form – is relatively bioinert and chemically stable. Hence, an iodinated aromatic co-crosslinker that could be covalently incorporated into PCL networks would address the above-mentioned challenges. The absence of such a co-crosslinker has hampered the further development of biodegradable patient-specific implants entering clinical applications. Recently, we reported on a radiopaque monomer, AATIPA, which was covalently incorporated into 3D-printed gelatin-based hydrogels.[26] In addition, AATIPA is, due to the acidic carboxylic moieties, normally prevailingly anionic at physiological pH and highly polar, which is advantageous if acceleration of hydrolysis is needed. Moreover, three iodine atoms per monomeric unit strongly increase the local average Z, which increases materials' radiopacity.

Herein, we aim to covalently incorporate AATIPA into photo-crosslinked PCL networks to introduce radiopacity and detectability in X-ray and computed tomography. To this end, AATIPA will be covalently incorporated into a recently developed and tuneable material platform based on thiol-ene photo-crosslinkable PCL.[6,7] PCL networks have been developed through orthogonal thiol-ene chemistry, combining low polydispersity alkene-functionalized PCL with a tetra-functional thiol crosslinker. This approach offers superior mechanical properties in terms of brittleness compared to conventional acrylate-functionalized PCL, which remains the gold standard to date.

In this study, we describe the effect of the covalent incorporation of AATIPA on light-induced crosslinking as well as the resulting physicochemical properties of the radiopaque thiol-ene crosslinked PCL networks. We show that the biodegradation rate of the crosslinked materials can be tuned by manipulation of the AATIPA content, while no cytotoxicity related to the incorporation of AATIPA was observed. It is illustrated that the covalent incorporation of AATIPA increases the radiopacity of crosslinked PCL networks paving the way toward non-invasive in vivo imaging of biodegradable materials serving tissue engineering. To further validate the potential of these materials to serve tissue engineering applications, we employed (advanced) 3D printing techniques, including indirect and volumetric 3D printing, to demonstrate their printability. The indirectly printed samples were implanted into mice to evaluate the detectability of the AATIPA-enriched constructs in vivo, with degradation being observed over six months.

2. Experimental Section

2.1. Materials

ϵ-Caprolactone (> 99%) was supplied by Tokyo Chemical Industry (TCI, Tokyo, Japan). Allyl isocyanate (98%), ethylene glycol (anhydrous, 99.8%), pentaerythritol tetrakis(3-mercaptopropionate) (> 95%), tin(II) 2-ethylhexanoate (92.5 to 100%), dimethyl terephthalate (99.93%), Dulbecco's Modified Eagle Medium (DMEM), 10 v/v% fetal bovine serum, 2 v/v% calcein-acetoxymethyl (Ca-AM), propidium iodide (PI), NaOH (>97%), 5-amino-2,4,6-triiodoisophthalic acid (95%), diphenyl(2,4,6-trimethylbenzoyl)phosphine oxide (DPPO), (2,2,6,6-tetramethylpiperidin-1-yl)oxyl or (2,2,6,6-tetramethylpiperidin-1-yl)oxidanyl (TEMPO), and $CDCl_3$ were supplied by Sigma–Aldrich (Diegem, Belgium). Acrylic anhydride (≥ 90%, 500 ppm MEHQ as a stabilizer) was purchased from Fluorochem (Derbyshire, UK). Dimethyl formamide (DMF, 99.85%) was purchased at Acros (Geel, Belgium). Ethyl(2,4,6-trimethylbenzoyl) phenylphosphinate (Speedcure TPO-L, 94.5%) was supplied by Lambson Ltd HQ (West Yorkshire, UK). Toluene (> 99%), chloroform (stabilized with amylene, > 99%), and diethyl ether (stabilized with 5–7 ppm BHT, > 99%) were supplied by Chem-lab NV (Zedelgem, Belgium). Deuterated chloroform (stabilized with silver foils + 0.03% TMS, 99.8%) was supplied by Eurisotop. Deionized water used in all experiments (resistivity less than 18.2 MΩ cm) was prepared using an Arium 611 (Sartorius, Goettingen, Germany) with the Sartopore 2 150 (0.45 + 0.2 µm pore size) cartridge filter.

ϵ-Caprolactone was dried over calcium hydride (CaH_2) and vacuum distilled (120 °C, 10 mbar). Toluene was distilled over sodium with benzophenone as an indicator and subsequently stored on molecular sieves (4 Å). Acrylic anhydride was stored in the refrigerator at ≈4 °C. All iodinated compounds were protected from direct light. The remaining chemicals were used as they were purchased without any additional purifications.

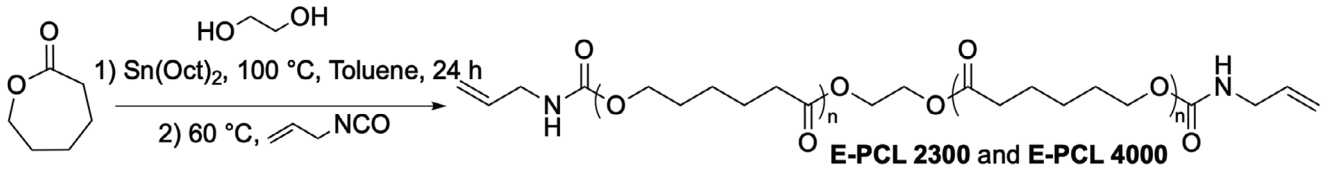

Figure 1. Synthesis of allyl-functionalized PCLs (PCL-(allyl)$_2$).

2.2. Methods

2.2.1. Synthesis of 5-Acrylamido-2,4,6-Triiodoisophthalic Acid (AATIPA)

The synthesis was prepared as previously reported.[26] Briefly, 5-amino-2,4,6-triiodoisophthalic acid (4.80 g, 8.16 mmol assuming the 95% purity as declared by the vendor) and dry acetonitrile (140 mL) was transferred to a dry round bottom flask. Afterward, a reflux condenser was attached and flushed the apparatus with inert gas (3 cycles of vacuum-nitrogen cycles). Subsequently, the flask was cooled with an ice bath and concentrated sulfuric acid (98%, 10 µL, 0.10 mmol) and acrylic anhydride (3.1 mL, 3.3 g, 23.6 mmol assuming 90% purity as claimed by the vendor) was added dropwise to the mixture. Afterward, the reaction mixture was slowly heated to 80 °C and the flask was heated for 63 h, during which the reaction mixture turned white. Then, the reaction mixture was cooled to room temperature, the reaction mixture was filtered and washed with cold acetonitrile (≈3 × 10 mL, three times). The product was isolated as a dry white powder, 4.47 g (94%).

^{1}**H NMR** (400 MHz, disodium salt in D_2O) δ: 6.51 (dd, J = 17.2, 10.1 Hz, 1H), 6.41 (dd, J = 17.2, 1.3 Hz, 1H), 6.01 (dd, J = 10.1, 1.3 Hz, 1H).

^{13}**C NMR** (101 MHz, disodium salt in D_2O) δ: 175.90, 167.44, 160.24, 154.85, 141.25, 130.01, 129.37, 91.45, 83.97.

2.2.2. Synthesis of Poly(ε-Caprolactone) with Allyl End Moieties (PCL-(allyl)$_2$)

Allyl-functionalized PCLs was prepared (2300 and 4000 g mol^{-1}, referred to as E-PCL 2300 and 4000, respectively), as previously described (**Figure 1**).[6]

First, ϵ-caprolactone (1.0 equiv.), tin(II) 2-ethylhexanoate ($Sn(Oct)_2$, 0.5 *wt.* % of added ϵ-caprolactone), ethylene glycol (1:17, and 1:34 initiator-to-monomer ratio for PCL 2300 and 4000, respectively), and anhydrous toluene (4 M concentration of ϵ-caprolactone) was mixed in a flask under argon atmosphere. Next, air was removed from the reaction flask by three freeze–pump–thaw cycles. Subsequently, the reaction mixture was stirred at 100 °C for 24 h (the full conversion was monitored with ^{1}H NMR). The obtained PCL-diols were further modified to alkene-functionalized PCLs by direct addition of 1.2 eq. of allyl isocyanate to the polymerization mixture and the reaction was stirred for 1 h at 60 °C (the conversion was monitored with ^{1}H NMR). The products were precipitated by pouring the reaction mixture into diethyl ether and isolated as a white solid.

The degree of substitution (DS) was determined as previously described by ^{1}H NMR spectroscopy ($CDCl_3$, Bruker Avance 400 MHz NMR Spectrometer), using dimethyl terephthalate (DMT) as an internal standard.[6] The respective PCL oligomer (10 mg) was dissolved in deuterated chloroform, and a ^{1}H-NMR spectrum was recorded. NMR spectra were analyzed in MestReNova, and the fully automated baseline correction (Whittaker Smoother) was applied. The integration of the initiator's methylene moiety (4.2 ppm) was set to 4, leading to integration values of the —(CH_2)— protons of PCL (4 ppm) being 37.7 for E-PCL 2300 and 76.0 for E-PCL 4000. These values were subsequently divided by 2 (the number of protons per repeating unit) to determine the number of repeating units (n_{PCL}). The molar mass was then calculated using the following formula:

$$M_n\ \left(g.mol^{-1}\right) = n_{PCL} * 114.14\ g.mol^{-1} + 2 * 83.09\ g.mol^{-1} + 62.07\ g.mol^{-1} \quad (1)$$

To determine the alkene content, dimethyl terephthalate (DMT, 10 mg, 0.05 mmol, 1 eq., M = 194.18 g mol^{-1}) was added as an internal ^{1}H-NMR standard along with 10 mg of the respective PCL precursor to CDCl3. NMR spectra were analyzed using MestReNova software, and the fully automatic baseline correction (Whittaker Smoother) was applied. The alkene content was calculated as follows:

$$Alkene\ content\ \left(mol.g^{-1}\right) = \frac{I(\delta 5.2) + I(\delta 5.8)}{I(\delta 8)} * \frac{N(DMT)}{N(alkene)} * \frac{m(DMT)}{MM(DMT)} * \frac{1}{m(EUP - PCL)} \quad (2)$$

2.2.3. Preparation and Characterization of Cross-Linked Materials

A range of characterization techniques was employed to determine the effect of the addition of AATIPA on the properties of the final materials. The crosslinking efficiency was determined by GF and HR-MAS, while the density of the crosslinked network was determined by SR in DMF. The effect of AATIPA on degradation temperature, crystallinity, and the melting point of the final material was determined by TGA and DSC. At last, the mechanical properties of the final material were determined via tensile testing. Additionally, the degradation of the materials was monitored in accelerated conditions (5 M NaOH) and physiological conditions (PBS buffer, pH 7.4). The results from the characterization of the crosslinked materials with AATIPA (samples **P1-P6**) were compared to control samples without AATIPA (samples **C1** and **C2**). Extensive statistical composition-to-property analysis had been performed (Section S10, Supporting Information) to evaluate these results.

Table 1. Mass/molar amounts of modified PCLs, groups with the double bonds, AATIPA monomer (m_{AATIPA}), and the molar ratios between AATIPA monomer and double bonds from an allyl-end group of selected PCLs (n_{AATIPA} /n_{ene}).

PCL-$(allyl)_2$	Code	Colour code	m_{AATIPA} [mg]	n_{AATIPA} [mmol]	$m_{PCL\text{-}(allyl)2}$ [g]	n_{ene} [mmol]	n_{AATIPA} /n_{ene}
E-PCL 2300	**C1**		0	0.000	1.0	0.748	0.000
E-PCL 2300	**P1**		40	0.066	1.0	0.748	0.094
E-PCL 2300	**P2**		80	0.131	1.0	0.748	0.189
E-PCL 2300	**P3**		160	0.262	1.0	0.748	0.378
E-PCL 4000	**C2**		0	0.000	1.0	0.501	0.000
E-PCL 4000	**P4**		40	0.066	1.0	0.501	0.131
E-PCL 4000	**P5**		80	0.131	1.0	0.501	0.262
E-PCL 4000	**P6**		160	0.262	1.0	0.501	0.524

2.2.4. Preparation of Cross-Linked Materials

The corresponding amounts of PCL-$(allyl)_2$ and AATIPA monomer (**Table 1**) were mixed and dissolved in DMF (0.45 mL to 1 g of PCL) at 50 °C in a dark glass vial to protect from light. The solution was sonicated to ensure proper mixing of all components and bubbled with argon. When all the components were dissolved and mixed, the TPO-L initiator (10 mg in each crosslinking solution), and the pentaerythritol tetrakis(3-mercaptopropionate) (1.0 eq. respectively to the double bonds in the corresponding E-PCL) were added to the mixture (exact molar amounts are overviewed in Table 1). The resulting solutions were bubbled with argon once more (for 1 min) and either used for in situ rheology or injected between two parallel glass plates covered with a thin poly(tetrafluoroethylene) sheet and separated by a 350 µm (for a cytotoxicity assay), or 1 mm (the rest of the experiments) thick silicone spacer. Next, the molds were irradiated from both sides with UV light (365 nm, 100 mW cm^{-2}) for 30 min. The obtained films were washed with DMF and overnight dried in a desiccator under vacuum for another 3 days to obtain yellow films, herein referred to as **P1**, **P2**, **P3** (materials containing E-PCL 2 kDa), and **P4**, **P5**, **P6** (materials containing E-PCL 4 kDa). The yellow color is likely caused by the presence of trace amounts of elemental iodide, whose generation could be reduced by removing the oxygen with argon before cross-linking. This yellow color of films could be washed away by swelling the films in dimethylformamide (DMF) overnight as described in the procedure.

2.2.5. Gel Fraction

To measure gel fraction, a sample of crosslinked PCL film (diameter 8 mm) was freeze-dried immediately after polymerization and measured its weight ($m_{d,2}$). Afterward, this dry material was incubated in DMF for 24 h, and the supernatant was removed. After this washing, the cross-linked gel was freeze-dried again and weighed ($m_{d,2}$). The gel fraction was determined by Equation (3). GF was determined in 3 independent measurements and reported as mean ± standard deviation (SD).

$$GF\ (\%) = \frac{m_{d,1}}{m_{d,2}} \cdot 100\% \tag{3}$$

2.2.6. Swelling Ratio in DMF (SR)

The equilibrium swelling ratio (SR) was determined using films with a diameter of 8 mm punched from the dried final crosslinked materials. The samples were let to swell in DMF for 24 h and then, the swollen mass (m_s) of the films was determined. Before weighing the samples, the excess DMF on the surface was gently removed using tissue paper. Afterwards, the samples were freeze-dried to determine the dry mass (m_d). The swelling ratio was then calculated using Equation (4). SR were determined in 3 independent measurements and reported as mean ± standard deviation (SD).

$$SR = \frac{m_s - m_d}{m_d} \cdot 100\% \tag{4}$$

2.2.7. High-Resolution Magic Angle Spinning (HR-MAS) ^{1}H-NMR Spectroscopy

^{1}H HR-MAS spectra of reactants were acquired to quantify their content of unreacted allyl/acrylamide moieties and equivalent spectra of products to confirm that all allyl/acrylamide moieties have extensively reacted. The ^{1}H experiments were recorded on a Bruker Ascend 500 MHz Avance III spectrometer equipped with a 4 mm ^{1}H/^{13}C Dual Channel HR-MAS probe, equipped with Z-gradients and running Topspin 3.6.5. For each measurement, the spinning frequency was set to 6 kHz, and all measurements were performed at room temperature (25 °C). Data were collected based on one sample per material type.

2.2.8. Elemental Analysis

The elemental analysis was conducted as described previously.[26] The C/H/N composition of freeze-dried hydrogels was measured using a PE 2400 Series II CHNS/O analyzer (Perkin Elmer, USA) in combustion mode (pure oxygen). The mass of all samples was 1.5 ± 0.1 mg (all samples were weighted with a calibrated scale with the certainty of 0.001 mg), The absolute uncertainty of CHN determination is ≤ 0.3 abs. %. The instrument was freshly calibrated before use. All samples were measured in 2 independent experiments.

The iodine content in freeze-dried samples was determined via the modified Leipert method.[26] The freeze-dried sample

(15 ± 1 mg, all samples were weighted with a calibrated scale with certainty of 0.01 mg) was placed into an ash-free filter paper, the filter paper was folded, attached to a glass stopper (ground glass joint, suspended with platinum wire) and inserted into a 500 mL conical flask. To this flask, we added an aqueous solution of sodium hydroxide (6 mL, 0.30 g of NaOH was dissolved in 6 mL of water). Afterward, this flask was flushed with pure oxygen, the ground-glass joint was sealed with a few drops of water (to reduce losses of iodine) and the sample was ignited. During the combustion, the stopper was held in place with force for a few seconds so that the stopper did not come loose and spill the content of the reaction flask (risk of explosion). Then, after 30 min (cooldown period) and 10 min of occasional shaking, the flask and stopper were washed with distilled water. During this reaction, elemental iodine (formed during the combustion) reacts with sodium hydroxide forming soluble salts of iodine (Equation 5), namely sodium iodide, and sodium hypoiodate, which then reversibly disproportionates into sodium iodide and sodium iodate (Equation 6).

$$I_2 + NaOH \rightarrow NaI + NaIO + H_2O \quad (5)$$

$$4NaIO \longleftrightarrow 3NaI + NaIO_3 \quad (6)$$

Subsequently, an aqueous solution of sodium acetate and bromine (15 mL, 3.00 g of sodium acetate trihydrate in 15 mL) was added. Next, a solution of bromine and sodium acetate was added in glacial acetic acid (at least 10 mL, more was added if needed until the reaction mixture was permanently orange, the solution consisted of 10.0 g of sodium acetate was dissolved in 100 mL of glacial acetic acid and a few drops of bromine were added so that the solution is notably orange). During this reaction, residual sodium iodide and hypo iodide were oxidized into sodium iodate (Equations 7 and 8).

$$NaI + 3H_2O + 3Br_2 \rightarrow NaIO_3 + 6HBr \quad (7)$$

$$NaIO + 2H_2O + 2Br_2 \rightarrow NaIO_3 + 4HBr \quad (8)$$

Then, the excessive orange color of the solution (due to excessive bromine) was removed by adding a few drops (1 to 2 drops) of formic acid until the solution was colorless (Equation 9).

$$Br_2 + HCOOH \rightarrow 2HBr + CO_2 \quad (9)$$

Finally, sulfuric acid (20 mL, 1.0 M), sodium iodide (≈1 g), and a solution of starch was added (Equation 10).

$$NaIO_3 + 5NaI + 3H_2SO_4 \rightarrow I_2 + 3H_2O + 3Na_2SO_4 \quad (10)$$

where elemental iodine formed a dark blue clathrate with starch. This solution was titrated with an aqueous solution of sodium thiosulfate (0.0333 M, Equation 11).

$$I_2 + 2Na_2S_2O_3 \rightarrow NaI + Na_2S_4O_6 \quad (11)$$

where equivalence was indicated by the discoloration of the solution.

The content of iodine in hydrogel (I_{wet}) was calculated with Equation (12):

$$I_{wet} = \frac{I_{dry}}{SR} \quad (12)$$

where I_{wet} is the content of iodine in the freeze-dried sample and SR is the swelling ratio of the hydrogel.

2.2.9. Thermogravimetric Analyses (TGA)

The TGA was conducted as described previously.[6] TGA of crosslinked materials (5–10 mg sample) was performed on TGA Q50 (TA instruments) with the heat ramp starting from 30 °C up to 750 °C at a heating rate of 10 °C min^{-1}. The degradation temperature was determined at a weight loss of 1.0, 5.0 *wt.*%, and the onset degradation temperature was evaluated (T_{onset}). Samples were measured in a platinum pan under a nitrogen flow of 60 mL min^{-1}. Data were collected based on one sample per material type.

2.2.10. Dynamic Scanning Calorimetry (DSC)

The DSC was conducted as described previously.[6] The DSC measurements of prepared materials were performed using a DSC Q2300 (TA Instruments) and RSC 500 cooler (Zellik, Belgium) employing ≈10 mg of the sample. A heating and cooling rate of 10 °C min^{-1} was used from −75 °C to 150 °C (first and third cycle), and from 150 to −75 °C (second cycle). The second heating and first cooling ramp were reported in the discussion related to the thermal properties, while the first heating ramp was reported in the discussion related to the mechanical properties. Each sample was measured in an aluminum Tzero pan under nitrogen flow and an empty pan was used as reference. The Q series software was used to analyze the DSC thermograms. Data were collected based on one sample per material type.

2.2.11. Tensile Testing

The tensile strength of materials was measured using a Tinius Olsen Model 1 ST apparatus, equipped with a load cell of 500 N using Horizon as software. Rectangular samples were cut from the crosslinked films (average length 14.0 mm, thickness 1.0 mm, and width 6.00 mm). An initial strain rate of 1 mm min^{-1} was used up to a force of 0.1 N after which the strain rate was increased to 10 mm min^{-1}. Measurements were performed in triplicate.

2.2.12. In Vitro Degradation

The in vitro degradation was conducted as described previously.[6] Accelerated (5 M NaOH, 37 °C) or physiological (140 mM, PBS, 37 °C) degradation assays were performed using 8-mm diameter discs (thickness of 1.0 mm), respectively. Measurements were performed in triplicate. At each time point, a disc was taken out of the solution, rinsed with water, dried with paper, and weighed to determine the remaining mass.

2.2.13. In Vitro Micro-Computed Tomography

The crosslinking solutions were crosslinked directly in the 1.5 mL Eppendorf vials. Afterward, the resulting crosslinked material was washed with DMF for 24 h (DMF was exchanged at least 5 times) to remove unreacted material. The material was dried in a desiccator for 4 days after which the micro-computed tomography (μCT) images were acquired with a preclinical X-CUBE micro-CT system (MOLECUBES, Ghent, Belgium), in "General-purpose mode" as previously described.[27] This mode encompassed a continuous scan, tube voltage 50 kV, tube current 75 μA, 480 projections (each projection has 1 averaging), acquisition per projection 125 ms, total acquisition time 90 s, dose per one-bed position 18 mGy. The X-ray source (X-ray tube) was a fixed tungsten anode with a 0.8 mm aluminum filter and a non-variable focal spot size of 33 μm. The flat-panel detector was based on CMOS technology (14-bits) using a CsI scintillator. It consists of 1536 × 864 pixels for an active area of 115 mm × 65 mm with a pixel size of 75 μm. Further hardware and software details were described in the previous article.[27] The mean value and standard deviation were obtained by generating cylindrical ROI in AMIDE-bin software (version 1.0.5). Data were collected based on one sample per material type.

2.2.14. Cytotoxicity Assay

The cytotoxicity assay was conducted as described previously.[6] Dulbecco's Modified Eagle Medium (DMEM) supplemented with 1 v/v% penicillin/streptomycin and 10 v/v% fetal bovine serum (FBS) was used to culture adipose-derived Stem Cells (ASC, Lonza) at 37 °C in 5% CO_2. The culture media was changed twice a week, and subculturing followed reaching 80 to 90% confluency up to a passage number of 5. A 70 v/v% ethanol solution was used to sterilize crosslinked films for cell culture through incubation for 24 h with a refreshment step after 12 h. Afterward, UV-C irradiation (100–280 nm, 20 mW cm^{-2} from both sides) was applied for 30 min. 10,000 ASC was seeded into the wells of a 96-well plate to initiate the direct contact biocompatibility assay. After one day, the sterilized samples were placed in direct contact on top of the cultured monolayer. The metabolic activity and viability of the monolayer were investigated through a 3-(4,5-dimethylthiazol-2-yl)−5-(3-carboxymethoxyphenyl)−2-(4-sulfophenyl)−2H-tetrazolium (MTS) and Live/Dead (Calcein-acetoxymethyl [CA-AM]/propidium iodide [PI]) assay, respectively, after one, three and seven days. After removal of the samples and the culture medium, a 17 *v/v*% MTS in the culture medium was added to the monolayer of cells and incubated in the dark at 37 °C for 1 h after which the absorbance was quantified at 490 nm with a spectrophotometer (Tecan Infinite M200 Pro) to quantify the cell metabolic activity. Moreover, a 2 *v/v*% CA-AM/PI in PBS solution was added to the monolayer of cells and incubated in the dark at room temperature for 10 min to quantify the cell viability. The cells were visualized through a green fluorescent protein (GFP) and a Texas Red (TxRed) filter of a fluorescence confocal laser scanning microscope (Carl Zeiss LSM 710). The percentage viability was computed using FIJI software. Measurements were performed in triplicate.

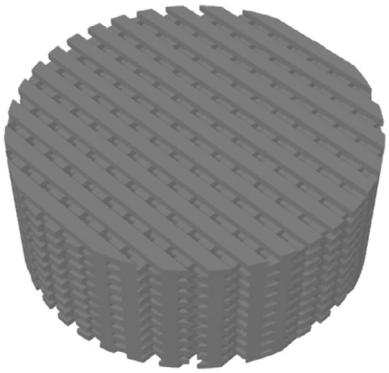

Figure 2. CAD design of PLA negative template.

2.2.15. Preparation of Negative Scaffolds and Indirect 3D-Printing of PCL Materials

The negative molds were printed out of polylactic acid (PLA) using an Anet A6 FDM printer. These molds were cylinder-shaped scaffolds with a meander-like pattern consisting of 10 layers, a total height of 3.7 mm, and a diameter of 8.4 mm (**Figure 2**).

The scaffolds were plasma treated using a FEMTO plasma reactor version 3 (Diener Electronic, Ebhausen Germany) for 2.5 min on each side with oxygen at a pressure of 0.8 mbar and a power of 100 W to render the PLA surface hydrophilic. Afterward, negative scaffolds were submerged into crosslinking solutions in dark vials, which were then placed under a vacuum to effectively suck the solutions into the pores of the negative scaffold. After 1 h under vacuum, the negative scaffolds filled with the crosslinking solution were taken out from the solutions, put on a 16-well plate, and irradiated from both sides with UV-A light (365 nm, 100 mW cm^{-2}) for 1 h. The obtained scaffolds were washed with chloroform to dissolve the PLA negative scaffold matric for 24 h (chloroform changed at least 5 times over 24 h) and then the resulting hydrogel scaffold was washed with washing solution (DMF) for 24 h (washing solution changed at least 5 times) and dried in a desiccator over the period of 3 days.

2.2.16. Scanning Electron Microscopy (SEM) of 3D Printed PCL Scaffold

The 3D-printed samples of PCL were dried for 3 days in a desiccator. Afterward, the samples were coated with the nano-layer of gold using an Automatic Sputter Coater K550X with an RV3 two-stage rotary vane pump (Emitech/Quorum Tech., East Sussex, UK). The images were obtained using instrument JCM-7000 NeoScope Benchtop SEM (JEOL Europe BV, Nieuw-Vennep, Netherlands).

2.2.17. In Vivo Imaging of the 3D-Porous Scaffold

These experiments were carried out following the Law of Animal Protection against Cruelty (Act No. 359/2012) of the Czech Republic, and they were conducted under an authority-approved protocol (MSMT-34384/2019–2). The animal house care adhered to the legislation on Experimental Work with Animals

(act No. 246/1992 of the Czech Republic and Decree No. 419/2012), fully complying with European Union directives.

An inbred Balb/c mouse (female, 12 weeks old) was used for the experiment. Surgery and CT examination were performed under isoflurane anesthesia (3% for initial and 1,5% for maintenance anesthesia). After the mouse was shaved, two scaffolds were implanted subcutaneously on the animal's back, each on one side of the body. Scaffolds were washed with organic solvent (DMF) before the experiment to remove possibly uncrosslinked material, dried in a desiccator, washed with ethanol:water solution (70:30 v/v), and incubated in sterile PBS for 24 h before implantation. Scaffolds were placed ≈1 cm from the entry incision, which was treated with tissue glue (Leukosan Adhesive). Subsequently, a CT scan was acquired using the CT modality of Albira PET/SPECT/CT Imaging System (Bruker Biospin, Ettlingen, SRN). The voltage of 45 kV and the current of 400 µA with an acquisition time of 30 min were used. After the end of CT scanning, the mouse was awake and had free access to water and food. Next CT acquisition was performed after 1 week. The image was reconstructed using of filtered back projection algorithm of Albira Software. For further image and data processing, PMOD software version 4.2 was chosen. Additionally, an ultrasound image to confirm the successful implantation has been taken directly after implantation, using an MX700 probe with a maximum penetration depth of 10 mm and higher resolution for further imaging (Figures S46 and S52, Supporting Information).

2.2.18. Volumetric 3D-Printing

A Tomolite v1.0 volumetric 3D printer from Readily3D (405 nm) was used to print 3D constructs. The resin was prepared according to the following procedure. E-PCL 2300 (0.75 g, 0.326 mmol) was dissolved in 128 µL THF. Subsequently, DPPO (22.5 µL, 2.58 µmol) from a stock solution of 40 mg mL^{-1} THF and TEMPO (45 µL, 1.15 µmol) from a stock solution of 4 mg/mL THF, were added to the solution. AATIPA (60 mg, 1.47 µmol) was dissolved in 128 µL THF. To ensure resin transparency, it was crucial to dissolve both PCL and AATIPA separately, before mixing. Subsequently, both solutions were mixed via sonication, vortexing, and heating. Next, pentaerythritol tetrakis(3-mercaptopropionate) (PETA-4SH, 141.10 µL, 0.37 mmol) was added to the solution followed by mixing until a homogeneous formulation was obtained. The mixture (0.8 mL) was transferred into a volumetric printer vial (outer diameter 9.90 mm, wall thickness 1.08 mm, Fisher, BK7), which was positioned in the volumetric printer. The I-WP30 3D design (4 mm x 4 mm x 3.6 mm) was uploaded to the Readily3D Tomolite printing software and correctly positioned within the vial (offset 4 mm in Z-direction). The absorption coefficient was set to 1.7 cm^{-2}, the refractive index to 1.45, and the dose to 625 mJ cm^2. After printing, the 3D construct was removed and transferred to a vial containing acetone. The acetone was replaced 3 times, after which DPPO (50 µL, from a stock solution of 20 mg mL^{-1} in acetone) was added and the structure was post-cured through UV-A irradiation at 365 nm for 30 min. Subsequently, the acetone was gradually replaced with isopropanol, which induced crystallization, thereby ensuring shape stability.

2.2.19. Data Processing and Statistical Analysis

At least 3 replicates were exploited in each experiment unless stated otherwise, and Excel (version 16.86 (24060916), Microsoft Corp., Richmond, WA, USA) build-in functions were utilized to obtain average values and standard deviations. The data were processed in OriginPro 2018 64-bit SR1 b9.5.1.195 (OriginLab Corporation, Northampton, MA, USA). The schemes and structures were drawn in ChemDraw Professional 16.0.1.4 (77) (Perkin Elmer Informatics, Inc., Waltham, MA, USA). All NMR spectra were processed using MestReNova version 12.0.0-20080 (Mestrelab Research S.L., Santiago de Compostela, Spain). The graphics were processed in Adobe Illustrator CS6 16.0.0 (Adobe Systems Inc., San Jose, CA, USA) and via BioRender.com. The data from the cytotoxicity study were processed with GraphPad Prism 8, version 9.5.0 (525), and were utilized to perform one-way variation analysis (ANOVA) and student's *t*-tests, on the obtained mean ± standard values. Results were considered statistically significant in case $p < 0.05$. Data from micro-CT were analyzed using AMIDE-bin software (version 1.0.5). The CT images were reconstructed using a filtered back projection algorithm of Albira Software. For further image and data processing, PMOD software version 4.2 was chosen.

2.2.20. Composition-Property Analysis

An analysis of the composition-property relationship was executed. In this analysis, the effect of the composition of the reaction mixture (n_{AATIPA}, amount of AATIPA in the reaction mixture, n_{ene}, alkene content in the reaction mixture, and n_{AATIPA}/n_{ene} ratio of molar amounts of ATIPA versus alkenes in the reaction mixture) was observed on the material final composition and properties, such as $w_{ATIPA,product}$ (wt. % of AATIPA in the final crosslinked material), I_{prod} (wt. % of iodine in the final crosslinked material), $n_{(AATIPA\ final)}/n_{(AATIPA\ initial)}$ (ratio between AATIPA content in final materials and initial AATIPA added to the formulation), RD (radiopacity), GF (gel fraction), SR (swelling ratio), *E'* (Young's modulus), Elong. Break (elongation at break), $T_{deg.}$ (degradation temperature), T_m (melting temperature), dH_m (enthalpy of melting), T_c (crystallization temperature), dH_c (crystallization enthalpy). A principal component analysis and correlation matrix were calculated using OriginPro 2018 (64-bit) SR1, b9.5.1.195 (OriginLab Inc. Northampton, MA, USA). The evaluated *p*-values mentioned in this manuscript, unless otherwise stated, were obtained from the mentioned principal component analysis.

2.3. Study Design

In this study, aim was to prepare a photo-crosslinkable PCL-based material with tuneable radiopacity. To this end, a photo-crosslinkable solutions was prepared that contained i) linear PCL with two terminal allyl moieties ($PCL(allyl)_2$, E-PCL) (characterization data included in Section S1, Supporting Information), ii) AATIPA monomer, iii) pentaerythritol tetrakis(3-mercaptopropionate) for step-growth thiol-ene crosslinking (**Figure 3**), and iv) photoinitiator TPO-L.

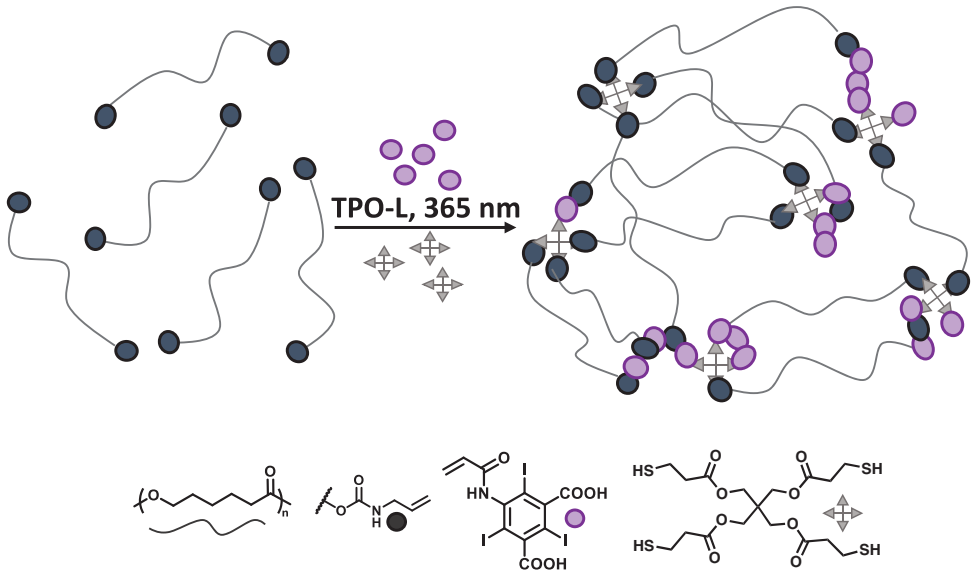

Figure 3. UV-initiated crosslinking of modified PCL in the presence of AATIPA monomer, tetrafunctional thiol, and photoinitiator. Notably, acrylamides can theoretically undergo a thiol-Michael reaction with tetrakis(3-mercaptopropionate) due to their alpha, beta-unsaturated carbonyl structure. However, this reaction is significantly slower than the radical thiol-ene reaction under the conditions used in this study (i.e., room temperature and absence of base/nucleophilic catalyst).[28] Additionally, in order to minimize any potential for thiol-Michael adduct formation, both compounds were added shortly before cross-linking.

The composition was carefully designed to meet the requirements for serving as light-based printable scaffolds in biomedical applications. First, PCL endows the materials with suitable biological and mechanical properties and makes them biodegradable. Second, AATIPA is a monomer with a high content of chemically stable iodine, thereby increasing the radiopacity of the final materials. Importantly, AATIPA does not absorb the wavelengths necessary for photo-crosslinking using common photoinitiators, such as TPO-L. Third, the terminal allyl moieties of PCL, acrylamide moieties in AATIPA, and pentaerythritol tetrakis(3-mercaptopropionate) permit light-based cross-linking of these materials in the presence of a photoinitiator.

At last, the effect of a) the content of hydrophilic AATIPA and b) the length of the PCL chain (molar masses of 2.3 and 4.0 kg mol^{-1}, E-PCL 2300, E-PCL 4000, respectively) was investigated on the physicochemical and biodegradation properties of the materials.

3. Results and Discussion

3.1. AATIPA Content Results in Lower Gel Fraction (GF) and Increases Swelling Ratio (SR) of Materials

Increasing the AATIPA content in the reaction mixture resulted in a decrease of the GF from 99% to ≈80% (**Table 2**, Pearson $p = 9.5\ 10^{-5}$, Figure S53, Supporting Information). This was confirmed with High-Resolution Magic Angle Spinning (HR-MAS) ^{1}H-NMR spectroscopy (Figures S10–S17, Supporting Information), which provides information about the residual number of crosslinkable groups (i.e., characteristic signals of the alkene

Table 2. Physico-chemical properties of crosslinked PCL: the content of iodine (I), and AATIPA (AATIPA) in the final product, the ratio between experimental and theoretical AATIPA content ($n_{AATIPA,exp}/n_{AATIPA,theor}$), gel fractions (GF), swelling ratios in DMF (SR), Young's moduli (E'), elongations at the break, and radiopacity (radiopacity, RD). Data are collected from 3 independent experiments. Mean ± standard deviations (SD) were obtained using Excel built-in functions.

Starting material	Code	Colour code	AATIPA [*wt.*%]	$n_{AATIPA,exp}/n_{AATIPA,theor}$	I [*wt.*%]	GF ± SD [%]	SR ± SD [%]	E' ± SD [MPa]	Elong. break [%]	RD [HU]
E-PCL 2300	C1		0.00	N/A	0.00	99.0 ± 0.7	340 ± 6	52.8 ± 7.8	589 ± 47	− 4 ± 207
	P1		4.12	1.14[a)]	2.56	93.2 ± 0.8		N/D[a)]	N/D[b)]	1193 ± 301
	P2		5.08	0.75	3.16	91.5 ± 0.6	465 ± 14	48.2 ± 13.4	628 ± 105	1548 ± 336
	P3		10.5	0.82	6.52	80.3 ± 3.5	654 ± 14	64.0 ± 7.7	582 ± 18	3005 ± 595
E-PCL 4000	C2		0.00	N/A	0.00	98.9 ± 0.5	408 ± 31	158 ± 21	671 ± 69	85 ± 202
	P4		2.84	0.83	1.77	94.1 ± 0.8	451 ± 3	N/D[b)]	N/D[b)]	1037 ± 285
	P5		5.72	0.86	3.56	90.1 ± 0.3	448 ± 15	130 ± 18	698 ± 58	1515 ± 530
	P6		11.4	0.92	7.07	85.1 ± 0.7	533 ± 20	143 ± 14	450 ± 28	3465 ± 998

[a)] The ratio of experimental and theoretical AATIPA content > 1 can be due to the release of non-crosslinked PCL during the washing procedure. [b)] To determine potential AATIPA addition altering the mechanical properties, only PCLs with higher AATIPA additions were tested.

Table 3. Evaluated degradation temperature (T_{onset}), crystallization temperature (T_c), crystallization enthalpy (ΔH_c), melting temperature (T_m), and melting enthalpy (ΔH_m).

Sample	T_{onset} [°C]	T_m [°C]	ΔH_m [J g^{-1}]	T_c [°C]	ΔH_c [J g^{-1}]
C1	322	20.2	37.3	9.22	33.8
P1	334	20.4	37.2	17.9	34.3
P2	308	22.7	30.0	8.20	10.3
P3	276	27.2	14.4	–	–
C2	352	40.6	45.4	18.7	47.8
P4	363	44.6	60.1	30.2	62.6
P5	360	42.0	46.8	21.7	49.5
P6	334	42.1	43.6	21.1	44.7

groups δ 5.8 ppm) within the materials, post-crosslinking. For the control materials **C1** and **C2** (without AATIPA), the conversion of alkene moieties is ≈100%. However, for the AATIPA-containing materials, the conversion of alkene moieties ranges between 85 and 92%, illustrating a slight reduction in crosslinking efficiency compared to the controls. This reduction can be explained by the deviation from the stoichiometric thiol:ene ratio, resulting from the introduction of AATIPA.

In turn, increasing the AATIPA content in the reaction mixture increased the SR of the samples in DMF (Table 2, Pearson $p = 5.3\ 10^{-3}$, Figure S54, Supporting Information). On the one hand, this increase of SR is likely caused by oligo-/polymeric AATIPA linkers present between the crosslinking points, thereby increasing the mesh size between the crosslinking points, as well as increasing the hydrophilicity of the final material. Conversely, the observed swelling behavior may also be attributed to the aforementioned crosslinking efficiency. This phenomenon is exemplified by the similar swelling ratios (SR) of samples **P4** and **P5**, for which a comparable crosslinking efficiency is observed (Figures S15 and S16, Supporting Information) despite a two-fold increase in AATIPA content.

3.2. AATIPA has No Effect on the Materials' Cross-Linking Kinetics, Mechanical or Thermal Properties

We assessed the influence of the incorporation of AATIPA on the in situ crosslinking kinetics through photo-rheology (Figures S2–S9, Supporting Information) and found no significant effect of AATIPA on the gel point. In other words, the addition of AATIPA to the ink does not compromise its photo-crosslinking kinetics and is therefore hypothesized not to hamper the 3D-printing process.

Next, we observed that adding AATIPA to the reaction mixture has no significant effect on Young's modulus (E') nor the elongation at the break of the final materials (Table 2, Figures S34–S39, Supporting Information). The statistical analysis (Section S10, Supporting Information) shows that only an increasing molar content of the allyl moiety in the reaction mixture (n_{ene}) significantly decreases Young's modulus, which has been previously described to be the result of different crystallinity of the crosslinked PCL.[7] However, a decrease in storage modulus (G') in the case of materials **P4-P6** can be observed in in situ photo-rheology compared to the control sample **C2** (Figures S6–S9, Supporting Information). This illustrates that the mesh size is increased, which aligns with the increased swelling.[29] However, this impact on G' during photo-crosslinking had a negligible effect on the Young's modulus in the final, dried state, due to the crystallization of the samples.

Similarly, the AATIPA content had no significant effect on the thermal properties of the materials (melting point, crystallization temperature, and degradation temperature, **Table 3**, Section S5, Supporting Information). The only factor affecting the thermal properties is the higher n_{ene}, which significantly decreased the materials' melting point, crystallization temperature, and degradation temperature ($p < 0.05$ for all parameters, Section S5, Supporting Information). The n_{ene} is directly connected to M_c, or the molar mass between crosslinks, which was previously reported to be a critical factor affecting the mechanical and thermal properties of a material.[6,7]

In conclusion, the covalent incorporation of AATIPA into the thiol-ene photo-crosslinked PCL networks does not affect their cross-linking kinetics, mechanical properties, or thermal properties.

3.3. AATIPA Accelerates the Hydrolysis of Crosslinked PCL

Thiol-ene photo-crosslinked networks are biodegradable via in vivo hydrolysis, which we studied using an in vitro "accelerated degradation" assay (5 M NaOH, 37 °C, **Figure 4A**) as well as in an assay mimicking physiological conditions (PBS buffer, pH 7.4, 37 °C, Figure 4B). The presence of AATIPA significantly increased the degradation rate, likely because of the presence of hydrophilic AATIPA facilitating water penetration into the bulk of the material. Catalytic effect of acidic carboxylic acid groups is also possible (in case of physiological conditions). Additionally, the hydrolysis rates of the crosslinked PCL-based materials decrease with decreasing n_{ene}, i.e., the abovementioned decreasing crosslinking density (**C1** compared to **C2**, **P1-P3** compared to **P4-P6**), corroborating a previous study, where this phenomenon is ascribed to increased hydrophilicity, and thus, swelling in aqueous solvents due to the used crosslinker.[7] Therefore, the incorporation of AATIPA into the materials can be a means to tune their biodegradation rate and thus may broaden the scope of applicability of PCL-based materials. The effects of AATIPA and n_{ene} on the degradation rates can be observed in the accelerated degradation profiles. The slow degradation profile illustrates the initial

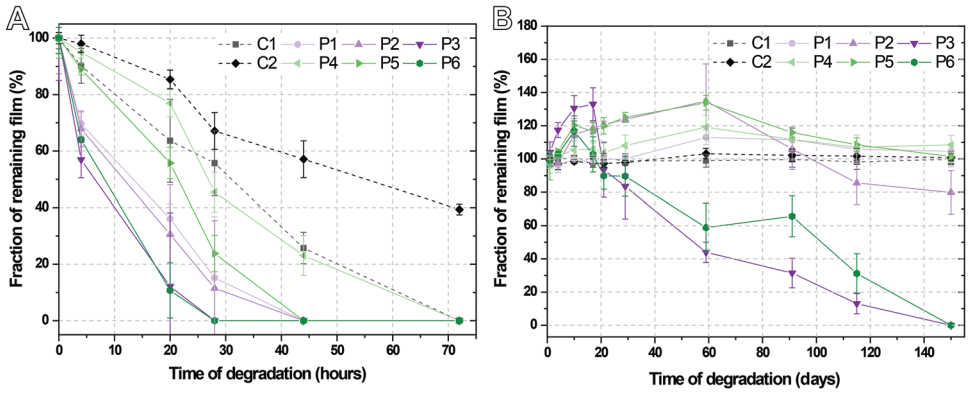

Figure 4. Effect of AATIPA monomer addition on the properties of PCL materials crosslinked via step-growth polymerization: A) accelerated degradation using 5 M NaOH, and B) slow degradation in physiological conditions (140 mM PBS buffer, pH 7.4, 37 °C). The materials with increasing AATIPA content based on E-PCL 2300 (**P1-P3**) and E-PCL 4000 (**P4-P6**) are compared to the control groups: crosslinked E-PCL 2300 (**C1**) and E-PCL 4000 (**C2**) without AATIPA. Data were collected from 3 independent experiments. Mean ± SD values were obtained using Excel built-in functions.

swelling of PCL, followed by the gradual decrease of the mass. Notably, after long-term exposure of the material to air, the material also became brittle, possibly due to oxidative degradation of the thioethers in the air.[30]

3.4. Increasing Content of AATIPA Increases the Radiopacity

The incremental incorporation of AATIPA into the thiol-ene photo-crosslinked PCL networks led to a linear increase of the iodine content present in the final material (Figure S55, Supporting Information, Pearson p-value = $1.5{\cdot}10^{-6}$). By comparing the final AATIPA content, covalently incorporated into the networks (i.e., present after washing), with the amount of AATIPA initially introduced, we found an incorporation efficiency of> 80% for most materials. This corresponded with AATIPA concentrations ranging from 2.8 up to 11.4 *wt.* % (Table 1). Importantly, the linear increase of the iodine content was shown to significantly increase the radiopacity (Figure 6A, Table 1, Pearson p-value = $2.0{\cdot}10^{-7}$). This increase in radiopacity is put into perspective in Figure 6B, where we compare the radiopacities of photo-crosslinked PCLs and various tissues[31] as well as examples of various materials[32,33] adapted from literature, measured under similar conditions. It is important to note, that the experimental setups used in this study are limited to X-ray energies < 50 keV, comparably to as they are used in plain X-ray imaging. For the most common CT scanners in clinical practice, higher energies (usually 90–100 kV) are used.[34] With increasing radiation energy, the ratio of the attenuation coefficient of AATIPA relative to that of water decreases (Figure S40, Supporting Information). Therefore, with higher radiation energy (e.g., 100 keV), the AATIPA would provide lower contrast to the surrounding environment than at lower radiation energies (e.g., 50 keV). Nevertheless, even at 100 keV, the attenuation is still significantly higher than that of water or bone. Therefore, our implants would provide sufficient signal, even when using clinical CT scanners.

In summary, by altering the content of AATIPA in the thiol-ene photo-crosslinkable formulations, we can predict and tune the radiopacity of the final materials, and thus tune their detectability in radiological imaging techniques.

3.5. AATIPA Content does not Impair the Biocompatibility of PCL-Based Materials

Biocompatibility of the developed materials was tested in a live/dead assay, during which adipose-derived stem cells were cultivated in direct contact with the crosslinked films (**Figure 5**). The measured materials (with the highest AATIPA content, **P5**, and **P6**, compared to the sample without AATIPA, **C2**) did not show any signs of cytotoxicity.

3.6. In Vivo Visualization of Photo-Crosslinked PCLs

Given the promising mechanical properties of the developed scaffolds and their potential application in bone tissue engineering, the radiopacity of the material must surpass that of bone to ensure sufficient contrast for imaging. As illustrated in **Figure 6D**, scaffolds with intermediate AATIPA loading already provide adequate contrast with both cortical and trabecular bone. Additionally, even the lowest AATIPA loading is sufficient to serve applications in trabecular bone tissue engineering. Based on these findings, porous 3D scaffolds were fabricated from a selected material with optimal radiopacity (**P2**, RD ≈1500 HU) and a control sample (**C1**) using indirect 3D printing with PLA-based negative molds (Figures 1 and 6B).

The negative scaffolds were designed to have sufficiently large pores (500 µm) to allow for cell proliferation, diffusion of nutrients, and waste exclusion. The scaffold morphology was determined by scanning electron microscopy (Section S8, Supporting Information). The 3D porous scaffolds were implanted subcutaneously through an incision in the lower abdominal area of a mouse (**P2** on the left side, non-detectable **C1** control on the right side) and visualized in vivo via CT scanning (Figure 6C and Section S8, Supporting Information). We showed that the **P2** scaffold can be visualized via CT, while the **C1** control group without

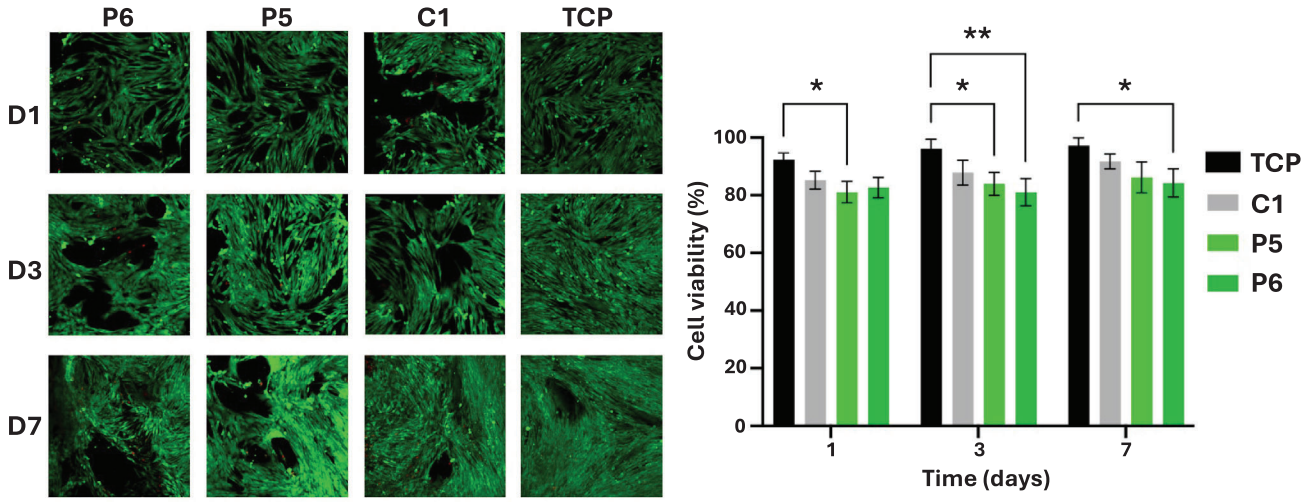

Figure 5. Adipose-derived stem cells cultivated with (**C1**, **P5**, and **P6**) or without (TCP) crosslinked films. Live/dead staining was evaluated on days 1, 3, and 7 after seeding. GraphPad Prism 8 was utilized to perform one-way variation analysis (ANOVA) and student's t-tests. Results were considered statistically significant in cases $p < 0.05$ (*) and $p < 0.01$ (**).

the incorporated contrast agent cannot be visualized in vivo. The latter evidences the great potential of the herein-developed material platform for the fabrication of in vivo detectable PCL scaffolds.

The scaffolds were remeasured 8 and 173 days after implantation. The volume of the scaffold containing AATIPA (**P2**) was easily determined, allowing a decrease to less than half of its original size (fraction of the remaining scaffold of 39.8%, **Figure 7**, Table S2, Supporting Information). This result can be compared with the in vitro degradation assay (Figure 4, Table S2, Supporting Information), where the degradation of **P2** in PBS was observed after 150 days, leaving 80.0 ± 13.1% of the non-degraded fraction of the sample. Apart from the significant decrease in the scaffolds' volume, the average radiopacity seemingly increased (Table S2, Supporting Information). The average RD is influenced by the scaffold's porosity. Therefore, an increase in RD may indicate a shrinking/collapse of pores. However, fluctuations in the average RD may generally be attributed to experimental errors arising from the irregularity of the scaffold's porous structure. Nevertheless, since the RD did not significantly decrease while the scaffold volume did, it is likely that surface degradation, rather than bulk degradation, occurred. Additionally, we show that sonography (ultrasound imaging) can reliably visualize the implants if they are near the body surface (Figures S46–S52, Table S2, Supporting Information). The ultrasound data confirmed the decrease in the **P2** scaffold volume (the fraction of remaining scaffold was equal to 10.4%), while the **C1** scaffold volume fluctuated around the value measured a day after implantation. However, a long-term in vivo degradation study with a statistically significant sample size is needed to accurately determine the half-life of the developed materials.

In conclusion, our proof-of-concept in vivo detectability study demonstrates that our samples can be visualized in vivo. The incorporation of AATIPA enhances contrast with surrounding tissues, enabling accurate volume determination. Additionally, the developed samples can be visualized using ultrasound imaging. However, the limitation of the penetration depth has to be taken into account. We confirmed that the incorporation of AATIPA accelerates the degradation of crosslinked PCL.

3.7. Proof-of-Printability via Volumetric 3D-Printing

3D printing has transformed tissue engineering by enabling the production of high-resolution, patient-specific implants (PSIs) with controlled porosity. These implants are vital for achieving an optimal anatomical fit, enhancing tissue integration, and minimizing post-operative infection risks while ensuring aesthetic quality.[35,36] Recently, volumetric 3D printing has emerged, allowing for the rapid, volume-at-once production of PSIs with micrometer precision in less than a minute. This technique utilizes sequential 2D light projections delivered into a rotating resin vial, enabling the sterile, one-step fabrication of complex 3D constructs, regardless of size or design complexity.[37,38]

The crosslinking solution based on the **P2** sample, previously selected for in vivo evaluation, was selected as a photocrosslinkable resin for proof-of-concept processing with contrast agent incorporation via volumetric 3D printing. To ensure effective printing, the resin must remain transparent at 405 nm to minimize light scattering. Due to the slight opacity of the crosslinkable precursors being dissolved in DMF, THF was identified as an alternative solvent for volumetric 3D printing. Minimizing solvent volume is critical as well, as excessive amounts can reduce resin viscosity and cause objects to sink during printing due to an increased local density. Thus, optimizing the AATIPA-integrated resin necessitated balancing AATIPA solubility with viscosity, leading to the selection of a 67 *w/v*% E-PCL 2300 concentration in THF. The optimal photo-initiator concentration (DPPO, 2.3 mM) was established as well. However, the use of DPPO is constrained by the need for the light to pass through the entire diameter of the vial, which attenuates the light intensity. Given that the Tomolite software allows for the correction of a maximal absorbance coefficient of 2, the permissible photo-initiator concentration was determined to be 2.9 mM, which is

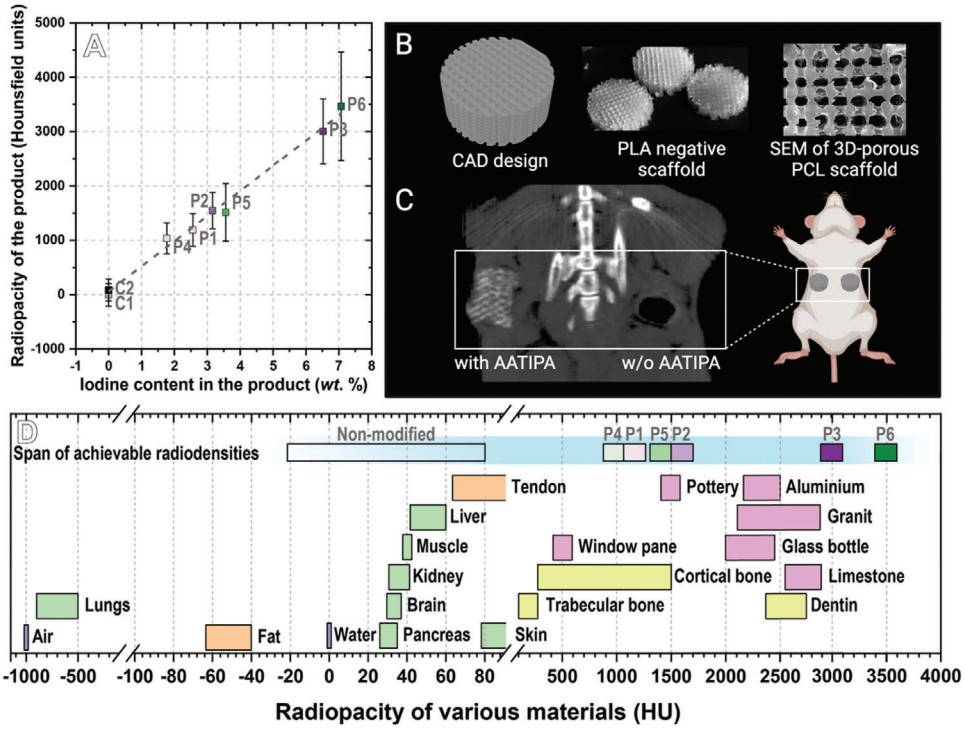

Figure 6. A) CT images of phantoms (vials) with polymer samples showing linear dependence of increasing iodine content on radiopacity expressed in Hounsfield scale (HU). The linear regression analysis was obtained using the built-in functions of OriginPro 2018. Data were collected from 3 independent experiments. B) CAD design of the negative scaffolds, image of PLA negative scaffolds, SEM micrograph of the resulting 3D-porous construct C) In vivo visualization of 3D-porous scaffold based on P2 crosslinked material (left side), compared to non-detectable 3D-porous scaffold based on control sample C1 (right side), 8 d after implantation. D) Comparison of radiopacities of samples, selected tissues, and materials. CSF represents the cerebrospinal fluid, Al stands for aluminum, and D stands for dentin. Radiopacities of tissues[31] and various materials[32,33] adapted from literature, were measured under similar conditions. The mean radiopacity ± SD was obtained using AMIDE-bin software for each measured sample.

well above the used DPPO concentration (i.e., 2.3 mM). Finally, to ensure an efficient printing process, the resin must exhibit a non-linear response to the absorbed irradiation and should have a distinct energy threshold, below which no significant polymerization takes place. Thus, to achieve said non-linear response, a nitroxide radical scavenger (TEMPO, 1 mM) was added to the thiol-ene-based photo-crosslinkable resin, which has already been proven effective for other thiol-ene-based resins.[7,39,40] In the absence of TEMPO, the obtained 3D constructs were either under- or over-cured.

The final formulation (66 *w/v*% E-PCL 2300, 2.3 mM DPPO, 1 mM TEMPO in THF, combined with 80 mg of AATIPA/1 g

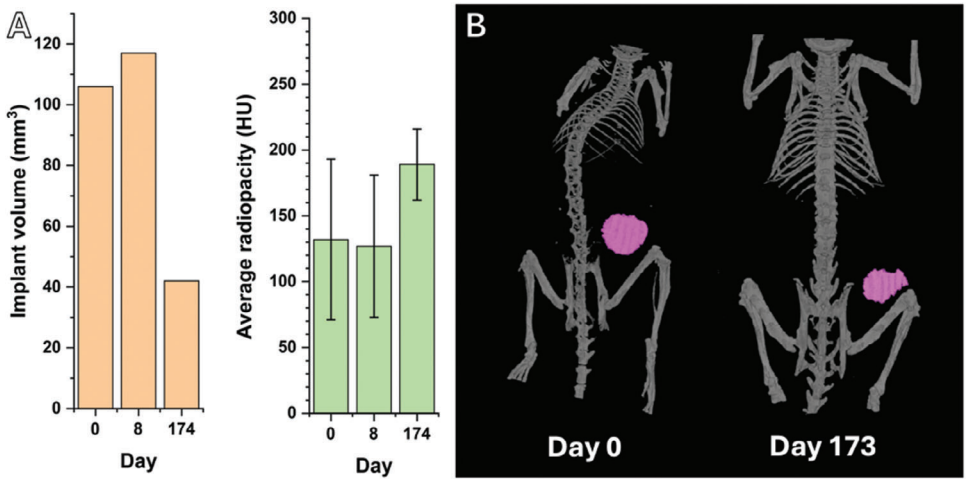

Figure 7. A) Volume and average radiopacity of an implant based on **P2** crosslinked material over time. The mean values ± SD were obtained using PMOD software version 4.2. B) 3D reconstruction from in vivo CT image (pink scaffold contains 5 wt.% AATIPA).

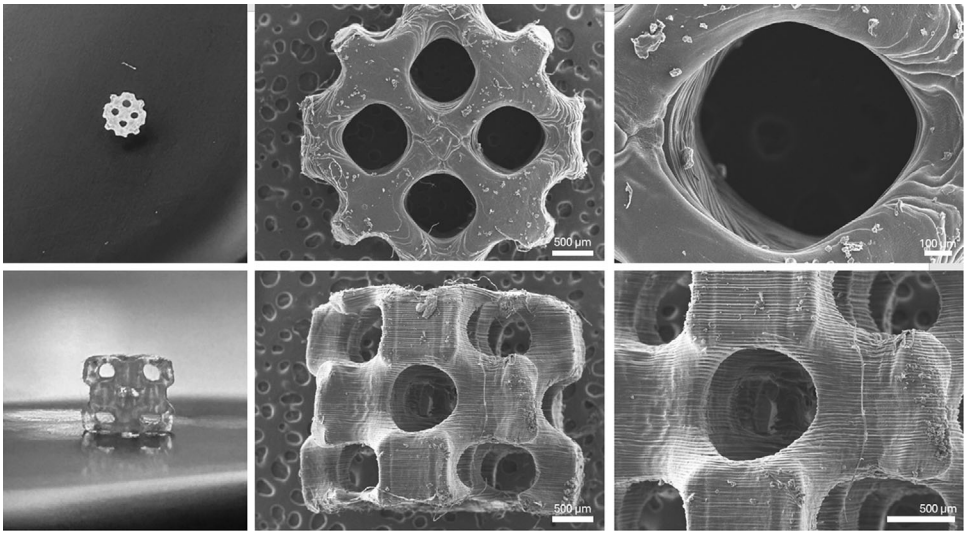

Figure 8. Pictures and SEM images of triply periodic minimal surface (I-WP30) structures, printed with a volumetric 3D printer.

of E-PCL) proved to be successful in generating triply periodic minimal surface (I-WP30) structures, as illustrated in **Figure 8**. Thus, by combining the precision and efficiency of volumetric 3D printing with the incorporation of AATIPA, we successfully managed to print complex, porous 3D designs of radiodense PCL in less than 1 min, enabling the potential in vivo monitoring of a patient-specific 3D construct as well.

4. Conclusion

AATIPA introduces radiopacity for PCL-based crosslinked materials. Increasing the AATIPA content in the reaction mixture increases the iodine content in the final material, thereby increasing its radiopacity, while not significantly affecting the mechanical properties of the crosslinked PCL. The resulting materials exhibited high mechanical strength with Young's moduli of 48.2 ± 13.4 up to 143 ± 14 MPa and elongations at break of 450 ± 28 up to 628 ± 105%. Furthermore, we found that the biodegradation rate can be accelerated via the incorporation of AATIPA monomer, which can broaden the scope of PCL-based biomaterials in the tissue engineering and regenerative medicine field. The resulting materials were proven to be non-cytotoxic and well-detectable in vivo via a conventional CT diagnostic technique. The biodegradability of the scaffold with incorporated AATIPA was confirmed, with a decrease of its volume down to 39.8% of its original size after 173 days following implantation. In the final stage, the 3D printability of a selected photo-crosslinkable formulation was confirmed via volumetric 3D printing. Therefore, our study provides guidelines for preparing biocompatible, biodegradable, PCL-based, radiopaque implants detectable in vivo via radioimaging.

Supporting Information

Supporting Information is available from the Wiley Online Library or from the author.

Acknowledgements

K.K. and Q.T. gratefully acknowledge the financial support provided by the Research Foundation—Flanders (FWO, Fonds Wetenschappelijk Onderzoek—Vlaanderen, Project 1229422N, 1SA2323N). S.V.V. acknowledges the Research Foundation – Flanders for providing a Hercules grant (I003922N) and VLAIO for financial support of an ICON project (HBC.2023.0736). J.H., PM., M.D. and L.S. acknowledge the grants LM2023050 Czech-BioImaging funded by the Ministry of Education, Youth and Sports of the Czech Republic, and SVV 260 635/ 2024 grant by Charles University. The authors thank the NMR expertise center at Ghent University for providing support and access to its NMR infrastructure. The 500 MHz instrument used in this work was funded by a grant from FWO (Project FWO I006920N). J.K. and M.H. thank the Ministry of Education, Youth and Sports of the Czech Republic (grant # LM2023053 EATRIS-CZ). The study was co-funded by the project New Technologies for Translational Research in Pharmaceutical Sciences/NETPHARM, project ID CZ.02.01.01/00/22_008/0004607, co-funded by the European Union. The authors also thank Prof. Christian Vanhove for help in the acquisition of micro-CT scans.

Conflict of Interest

The authors declare no conflict of interest.

Data Availability Statement

The data that support the findings of this study are available from the corresponding author upon reasonable request.

Keywords

computed tomography contrast agent, implant, light-based 3D printing, light-based crosslinking, photo-crosslinkable polymers, polyester, thiol-ene step growth polymerization

Received: June 20, 2024
Revised: October 24, 2024
Published online: November 19, 2024

[1] L. Li, D. V. LaBarbera, (Eds: S. Chackalamannil, D. Rotella, S. E. Ward), in *3D High-Content Screening of Organoids for Drug Discovery*, Elsevier, Oxford, England, UK **2017**, 388.
[2] M. Jafari, Z. Paknejad, M. R. Rad, S. R. Motamedian, M. J. Eghbal, N. Nadjmi, A. Khojasteh, *J. Biomed. Mater. Res. B Appl. Biomater.* **2017**, *105*, 431.
[3] S. H. Kim, Y. Jung, (Eds: M. W. King, B. S. Gupta, R. Guidoin) in *Biotextiles as Medical Implants*, Woodhead Publishing, Sawston, Cambridge **2013**, 91.
[4] B. D. Ulery, L. S. Nair, C. T. Laurencin, *J. Polym. Sci. B Polym. Phys.* **2011**, *49*, 832.
[5] B. Prediger, T. Mathes, C. Probst, D. Pieper, *Syst Rev.* **2020**, *9*, 225.
[6] Q. Thijssen, A. Quaak, J. Toombs, E. De Vlieghere, L. Parmentier, H. Taylor, S. Van Vlierberghe, *Adv. Mater.* **2023**, *35*, 2210136.
[7] Q. Thijssen, L. Parmentier, E. Augustyniak, P.-A. Mouthuy, S. Van Vlierberghe, *Adv. Funct. Mater.* **2022**, *32*, 2108869.
[8] Q. Thijssen, L. Parmentier, K. Van holsbeeck, S. Ballet, S. Van Vlierberghe, *Biomacromolecules* **2023**, *24*, 1638.
[9] F. Causa, E. Battista, R. Della Moglie, D. Guarnieri, M. Iannone, P. A. Netti, *Langmuir* **2010**, *26*, 9875.
[10] A. A. Appel, M. A. Anastasio, J. C. Larson, E. M. Brey, *Biomaterials* **2013**, *34*, 6615.
[11] S. Y. Nam, L. M. Ricles, L. J. Suggs, S. Y. Emelianov, *Tissue Eng. Part B Rev.* **2014**, *21*, 88.
[12] J. Fu, M. Wang, I. De Vlaminck, Y. Wang, *Small* **2020**, *16*, 2004133.
[13] J. Shi, S. Chen, L. Wang, X. Zhang, J. Gao, L. Jiang, D. Tang, L. Zhang, A. Midgley, D. Kong, S. Wang, *J. Biomed. Mater. Res. B Appl. Biomater.* **2019**, *107*, 2040.
[14] M. Sun, P. J. Kingham, A. J. Reid, S. J. Armstrong, G. Terenghi, S. I. Downes, *J. Biomed. Mater. Res. A* **2010**, *93A*, 1470.
[15] M. Shahrezaee, M. Salehi, S. Keshtkari, A. Oryan, A. Kamali, B. Shekarchi, *Nanomedicine* **2018**, *14*, 2061.
[16] S. H. Park, D. S. Park, J. W. Shin, Y. G. Kang, H. K. Kim, T. R. Yoon, J.-W. Shin, *J. Mater. Sci. Mater. Med.* **2012**, *23*, 2671.
[17] L. Jing, M. Sun, P. Xu, K. Yao, J. Yang, X. Wang, H. Liu, M. Sun, Y. Sun, R. Ni, J. Sun, D. Huang, *ACS Appl. Bio. Mater.* **2021**, *4*, 3189.
[18] S. H. Kim, J. H. Park, J. S. Kwon, J. G. Cho, K. G. Park, C. H. Park, J. J. Yoo, A. Atala, H. S. Choi, M. S. Kim, S. J. Lee, *Biomaterials* **2020**, *258*, 120267.
[19] X. Dang, N. M. Bardhan, J. Qi, L. Gu, N. A. Eze, C.-W. Lin, S. Kataria, P. T. Hammond, A. M. Belcher, *Sci. Rep.* **2019**, *9*, 3873.
[20] V. Crosignani, A. S. Dvornikov, J. S. Aguilar, C. Stringari, R. A. Edwards, W. W. Mantulin, E. Gratton, *J. Biomed. Opt.* **2012**, *17*, 116023.
[21] K. M. Pawelec, E. Tu, S. Chakravarty, J. M. L. Hix, L. Buchanan, L. Kenney, F. Buchanan, N. Chatterjee, S. Das, A. Alessio, E. M. Shapiro, *Adv. Healthcare Mater.* **2023**, *12*, 2203167.
[22] J. T. Martin, A. H. Milby, K. Ikuta, S. Poudel, C. G. Pfeifer, D. M. Elliott, H. E. Smith, R. L. Mauck, *Acta Biomater.* **2015**, *26*, 97.
[23] S. Houshyar, H. Yin, L. Pope, R. Zizhou, C. Dekiwadia, E. L. Hill-Yardin, J. M. C. Yeung, S. John, K. Fox, N. Tran, I. Cole, A. Elbourne, V. K. Truong, A. Truskewycz, *OpenNano* **2023**, *9*, 100120.
[24] J. V. D. Perez, B. Singhana, J. Damasco, L. Lu, P. Behlau, R. D. Rojo, E. M. Whitley, F. Heralde, A. Melancon, S. Huang, M. P. Melancon, *Materialia* **2020**, *14*, 100874.
[25] T. R. Olsen, L. L. Davis, S. E. Nicolau, C. C. Duncan, D. C. Whitehead, B. A. Van Horn, F. Alexis, *Acta Biomater.* **2015**, *20*, 94.
[26] O. Groborz, K. Kolouchova, L. Parmentier, A. Szabo, B. Van Durme, D. Dunlop, T. Slanina, S. Van Vlierberghe, *ACS Appl. Eng. Mater.* **2024**, *2*, 811.
[27] F. M. Muller, C. Vanhove, B. Vandeghinste, S. Vandenberghe, *Med. Phys.* **2022**, *49*, 3121.
[28] D. P. Nair, M. Podgórski, S. Chatani, T. Gong, W. Xi, C. R. Fenoli, C. N. Bowman, *Chem. Mater.* **2014**, *26*, 724.
[29] T. Canal, N. A. Peppas, *J. Biomed. Mater. Res.* **1989**, *23*, 1183.
[30] S. Adamek, D. Mackillop, H. Schnecko, *J. Appl. Polym. Sci.* **1972**, *16*, 2511.
[31] A. Kalra, (Eds: K.-H. Yang) in *Basic Finite Element Method as Applied to Injury Biomechanics*, Academic Press, Cambridge, MA, USA **2018**, 389–415.
[32] S. A. Bolliger, L. Oesterhelweg, D. Spendlove, S. Ross, M. J. Thali, *J. Forensic Sci.* **2009**, *54*, 1119.
[33] N. Emadi, Y. Safi, A. A. Bagheban, S. Asgary, *Iran Endod. J.* **2014**, *9*, 283.
[34] F. Tatsugami, T. Higaki, Y. Nakamura, Y. Honda, K. Awai, *Jpn J. Radiol.* **2022**, *40*, 547.
[35] R. N. Maniar, T. Singhi, *Curr. Rev. Musculoskelet. Med.* **2014**, *7*, 125.
[36] D. A. Zopf, C. L. Flanagan, A. G. Mitsak, J. R. Brennan, S. J. Hollister, *Int. J. Pediatr. Otorhinolaryngol.* **2018**, *114*, 170.
[37] I. Karakurt, L. Lin, *Curr. Opin. Chem. Eng.* **2020**, *28*, 134.
[38] B. E. Kelly, I. Bhattacharya, H. Heidari, M. Shusteff, C. M. Spadaccini, H. K. Taylor, *Science* **2019**, *363*, 1075.
[39] Q. Thijssen, J. Toombs, C. C. Li, H. Taylor, S. Van Vlierberghe, *Prog. Polym. Sci.* **2023**, *147*, 101755.
[40] C. C. Cook, E. J. Fong, J. J. Schwartz, D. H. Porcincula, A. C. Kaczmarek, J. S. Oakdale, B. D. Moran, K. M. Champley, C. M. Rackson, A. Muralidharan, R. R. McLeod, M. Shusteff, *Adv. Mater.* **2020**, *32*, 2003376.